Petroleum Science 23 (2026) 350–364

Contents lists available at ScienceDirect

Petroleum Science

journal homepage: www.keaipublishing.com/en/journals/petroleum-science

Original Paper

# Production performance of a post-fracturing elastoplastic model for deep shale gas reservoirs

Dong-Yan Fan [a,b], Can Yang [c], Hai Sun [a,b,*], Jun Yao [a,b], Xia Yan [a,b], Lei Zhang [a,b], Cun-Qi Jia [d], Gloire Imani [b], Si-Cen Lai [b], Liang Zhou [b]

[a] State Key Laboratory of Deep Oil and Gas, China University of Petroleum (East China), Qingdao, 266580, Shandong, China
[b] School of Petroleum Engineering, China University of Petroleum (East China), Qingdao, 266580, Shandong, China
[c] PipeChina Engineering Technology Innovation Co., Ltd., Tianjin, 300450, China
[d] Physical Science and Engineering Division, King Abdullah University of Science and Technology, Thuwal 23955-6900, Saudi Arabia

ARTICLE INFO

*Article history:*
Received 7 January 2025
Received in revised form
5 October 2025
Accepted 10 October 2025
Available online 22 October 2025

Edited by Yan-Hua Sun

*Keywords:*
Deep shale gas
Elastoplastic deformation
Flow and geomechanics coupling
Production performance

ABSTRACT

Deep shale gas reservoirs are characterized by high temperature, high pressure, and ultra-low permeability, making them highly susceptible to plastic deformation during hydraulic fracturing. In such cases, conventional elastic models fail to capture the complex post-fracturing rock behavior, highlighting the suitability of elastoplastic modeling. This study develops a fully coupled flow-geomechanics model incorporating elastoplastic deformation to analyze production performance in deep shale gas reservoirs. The proposed model dynamically couples post-fracturing plastic deformation with multiscale gas transport mechanisms, including slip flow, Knudsen diffusion, and surface diffusion. It incorporates governing equations that describe gas migration through the matrix, natural fractures, and hydraulic fractures, while simultaneously accounting for dynamic changes in effective stress, porosity, and permeability. Model validation is performed using the classical Mandel problem, followed by a detailed analysis of key parameters influencing elastoplastic production performance. Simulation results indicate that in elastoplastic reservoirs, production initially increases and then declines with increasing bottomhole pressure (BHP), while elastic reservoirs show a continuous increase. When the initial reservoir pressure is 50 MPa, elastic production dominates below BHP of 31.5 MPa, whereas elastoplastic production becomes more favorable above this threshold. A critical inflection point emerges when the BHP is approximately 0.5–0.625 times the original formation pressure. Furthermore, the most important influencing factors of elastic and elastoplastic formations are BHP and original formation pressure, respectively. These findings offer valuable insights into optimizing production strategies for deep shale gas reservoirs under complex geomechanical conditions.


## 1. Introduction

The development of deep shale resources is crucial for achieving global energy goals and transitioning to a carbon-neutral future. Despite mature technology for exploiting shallow shale gas reservoirs, over 60% of shale gas is located below 3500 m (Xu et al., 2021), posing greater challenges for extraction. Currently, development primarily relies on horizontal wells combined with hydraulic fracturing technology (Yu et al., 2022). Recent research on deep shale gas reservoirs reveals extensive plastic deformation in the near-wellbore zone during gas extraction, preventing the use of linear elasticity theory for stress changes as in shallow shale reservoirs. To achieve accurate production evaluation of deep shale gas, it is necessary not only to accurately describe the various flow mechanisms in deep shale gas reservoirs but also to have a clear understanding of the characteristics of post-fracturing plastic deformation of the rock.

Stress changes from hydraulic fracturing may activate pre-existing natural fractures and open micro-channels near the well, forming a complex hydraulic fracture network area

* Corresponding author.
*E-mail address:* sunhai@upc.edu.cn (H. Sun).
Peer review under the responsibility of China University of Petroleum (Beijing).

https://doi.org/10.1016/j.petsci.2025.10.005

(stimulated reservoir volume, SRV) (Bai et al., 2023). However, hydraulic fracturing in deep reservoirs under high temperature and high pressure can also cause extensive plastic deformation in the SRV area (Guo et al., 2020; Liu and Elsworth, 1999; Wang, 2020; Yao et al., 2018; Zhu et al., 2023). Many studies only consider stress changes based on linear elasticity theory, neglecting the impact of plastic deformation on the reservoir (Cao et al., 2016a; Hu et al., 2022; Liang et al., 2024; Shang et al., 2022; Shentu et al., 2024; Zhu et al., 2022). This method simplifies the stress field calculation but often overlooks dynamic changes in permeability and porosity due to plastic deformation. These changes directly affect production, so the impact of plastic deformation in deep reservoirs should not be underestimated (Karim et al., 2022; Kozhevnikov et al., 2024). Ran and Gu (1997) developed a 3D elastoplastic reservoir model, showing significant deviations in predicted pore pressure and effective stress when treating elastoplastic reservoirs as purely elastic. Some studies introduce elastoplastic constitutive equations to describe stress changes in deep shale gas reservoirs (Hu et al., 2019; Liao et al., 2024; Qi et al., 2021; Xing et al., 2020; Zeng et al., 2019) to study hydraulic fracturing effects. Yao et al. (2018) established a mathematical model for elastoplastic hydraulic fracture propagation based on the Drucker–Prager yield criterion and associated flow rules. Liao et al. (2024) developed a 3D finite element model for vertical hydraulic fracture propagation in deep shale reservoirs, using the Drucker–Prager elastoplastic model to analyze the impact of parameters like in situ stress on fracture morphology. Yi et al. (2025) proposed a dynamic fluid–solid coupled mixed-mode fatigue elastoplastic phase field model for simulating crack initiation and propagation in elastoplastic rocks under cyclic fluid loading. Most numerical simulations focus on crack propagation during hydraulic fracturing, with few studies linking hydraulic fracturing-induced plastic deformation to production processes to study the impact on post-fracturing production.

In fluid seepage processes, a continuous flow model is used to describe multiscale flow processes. Increasing gas production causes continuous shale deformation, causing changes in porosity and micro fractures, thereby resulting in the formation of different gas transport mechanisms such as gas slippage, Knudsen and surface diffusion. These transport mechanisms are linearly superimposed or weighted to obtain an apparent model of multiscale gas flow in shale. Javadpour (2009) proposed an apparent model for gas flow in shale reservoirs based on the linear superposition of surface diffusion and Knudsen diffusion. Li (2012) suggested that gas transport mechanisms in shale nanopores mainly involve continuous flow and Knudsen diffusion, superimposing these mechanisms according to their contributions. Wu et al. (2016) combined slip flow and Knudsen diffusion mechanisms according to their relative contributions to establish a comprehensive model considering surface diffusion and real gas effects. Zhang et al. (2018) derived expressions for the porosity sensitivity exponent and pore compressibility based on a dual porosity model, aiming to clarify the relationship between the stress sensitivity and pore structure of shale. In studying multiscale flow mechanisms of shale gas, many researchers propose coupling flow mechanisms with geomechanics and establishing mathematical models for porosity and permeability variations with effective stress based on the coupled theory proposed by Terzaghi (1943) and the more comprehensive consolidation theory further developed by Biot (1941, 1955). Jiang and Yang (2018) proposed a fully coupled model of fluid flow and geomechanics to simulate complex production phenomena in fractured shale gas reservoirs. Wei et al. (2021) proposed a discontinuous discrete fracture model for the coupling of seepage and geomechanics in fractured reservoirs based on the finite element method. It can be used to simulate the hydraulic fracturing of horizontal wells and the production process of shale oil reservoirs. Li and Liu (2023) established a general permeability model considering effective stress, gas adsorption, and flow regime effects. However, existing studies typically focus either on fracture propagation or couple flow with linear elastic geomechanics, often neglecting the impact of post-fracturing plastic deformation on long-term production. Although some models have incorporated elastoplastic behavior during fracture initiation, few have dynamically linked post-fracturing elastoplastic deformation with evolving multiscale gas flow mechanisms throughout the production stage. Moreover, current multiscale flow models rarely reflect the feedback loop between stress redistribution and flow parameters such as permeability and porosity in a plastic-deforming reservoir.

In this work, we address these gaps by developing a fully coupled elastoplastic flow-geomechanics model that dynamically captures stress-dependent variations in porosity and permeability under multiscale transport regimes. Unlike previous models, our approach integrates elastoplastic stress evolution with surface diffusion, slip flow, and Knudsen diffusion throughout the gas production lifecycle, providing a more realistic and accurate framework for deep shale reservoir performance evaluation.

The organization of this paper is as follows. Section 2 introduces the mathematical model considering post-fracturing plastic deformation. Section 3 introduces model validation and practical applications. Section 4 presents the results and discussion. The conclusion is in Section 5.

## 2. Model development

Our main objective is to develop the model of fractured horizontal well with post-fracturing elastoplastic deformation in deep shale gas reservoirs. In this section, a physical model and governing equations for shale deformation and gas flow are established, and dynamic coupling methods are discussed.

### 2.1. Physical model

Shale reservoirs have nanopores and natural fracture systems crucial for gas storage. Due to significant size differences in these features, gas migration involves complex multiphase mechanisms, including adsorption–desorption, Knudsen diffusion, surface diffusion, and gas slip. As illustrated in Fig. 1, gas molecules adsorb onto the shale matrix to form adsorbed gas and desorb into free gas when the reservoir conditions change. Simultaneously, free gas moves through Knudsen diffusion within the matrix towards natural fractures along the concentration gradient. Surface diffusion aids gas movement on the shale surface, facilitating overall migration. Gas near natural fractures then penetrates and accelerates transport via gas slippage. Finally, gas enters hydraulic fractures and is produced through horizontal wells.

The deformation of shale formations during extraction is shown in Fig. 2. During fracturing, continuous loading causes extensive plastic deformation around hydraulic fracture tips. During production, the continuous decline in gas pressure alters the effective stress field. The volume changes of shale due to gas adsorption and desorption are also considered. Deformation resulting from both production and fracturing ultimately leads to dynamic variation in reservoir permeability.

Clearly, deep shale gas development involves multi-physical processes. Cross-coupled equations dynamically link reservoir deformation and fluid seepage, illustrating system couplings as shown in Fig. 3. This paper will use a set of partial differential equations to derive mathematical models for each physical process, studying the coupling relationships between physical fields.

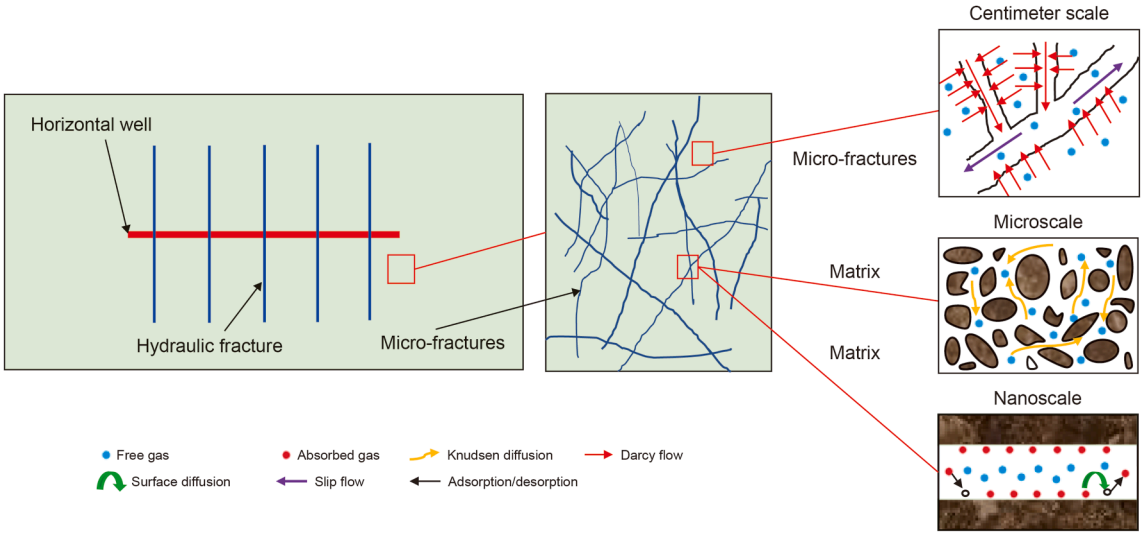


**Fig. 1.** Schematic diagram of multi-scale gas migration mechanisms in shale.

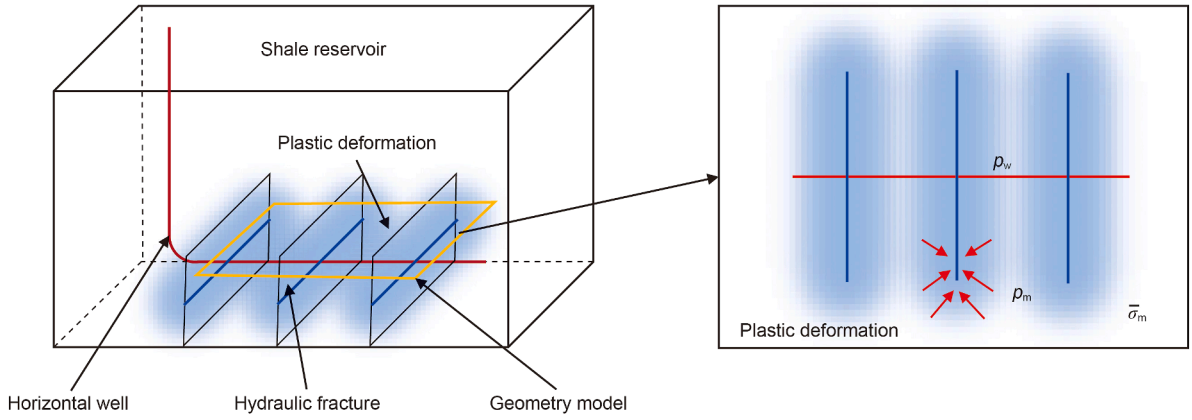


**Fig. 2.** Plastic deformation in shale reservoir.

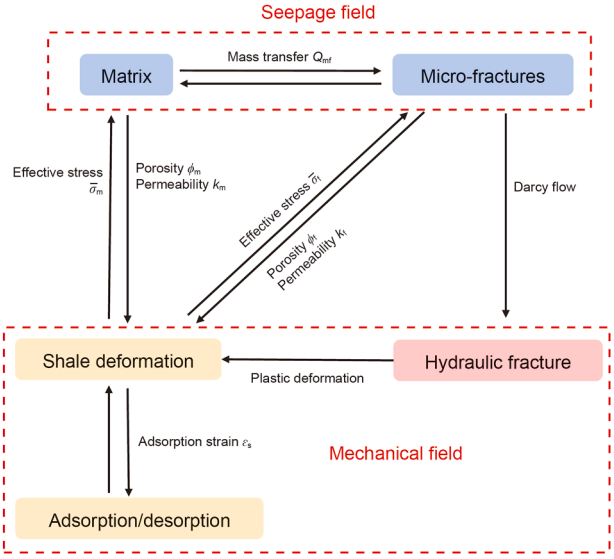


**Fig. 3.** Coupling relationships of multi-physical processes among different systems.

### 2.2. Governing equation of shale deformation

This section focuses on the plastic characteristics of shale rock. Combining the elastoplastic properties of the formation after fracturing and the elastic properties during production, a comprehensive elastoplastic model for deep shale gas hydraulic fracturing in horizontal wells is established.

#### 2.2.1. Elastic model for production processes

The stress field during production is described as elastic deformation. Considering the effect of pore fluid pressure on shale deformation, based on Biot's consolidation theory (Biot, 1955) and adsorption strain (Zhang et al., 2008), the constitutive equations for the matrix and natural fractures are as follows:

$$\begin{aligned}\boldsymbol{\sigma}_{ij} &= 2G_{\mathrm{m}}\varepsilon_{ij} + 2G_{\mathrm{m}}\frac{\nu_{\mathrm{m}}}{1-\nu_{\mathrm{m}}}\varepsilon_{\mathrm{kk}} - \alpha p_{\mathrm{m}}\delta_{ij} - K_{\mathrm{m}}\varepsilon_{\mathrm{s}}\delta_{ij} \\ \boldsymbol{\sigma}_{ij} &= 2G_{\mathrm{f}}\varepsilon_{ij} + 2G_{\mathrm{f}}\frac{\nu_{\mathrm{f}}}{1-\nu_{\mathrm{f}}}\varepsilon_{\mathrm{kk}} - \beta p_{\mathrm{f}}\delta_{ij}\end{aligned} \tag{1}$$

with $G = E/2(1+\nu)$, where subscripts m and f represent the shale matrix and natural fractures, respectively; $G$ is the shear modulus, Pa; $\nu$ is Poisson's ratio; $E$ is the Young's modulus, Pa; $p$ is pressure, Pa; $\alpha$ is the Biot coefficient of matrix; $\beta$ is the Biot coefficient of

natural fractures; $\varepsilon_{kk}$ is the volume strain; $\varepsilon_s$ is the adsorbed volume strain of shale matrix. The adsorption-induced volume strain is described by the modified Langmuir-type equation (Langmuir, 1968; Mehrabian and Abousleiman, 2015; Pan and Connell, 2012; Tuncay and Corapcioglu, 1995): $\varepsilon_s = \varepsilon_L p_m/(p_L + p_m)$. $\varepsilon_L$ is the maximum adsorptive volume strain of the matrix; $p_L$ is the Langmuir pressure constant for shale matrix.

#### 2.2.2. Elastoplastic model for post-fracturing

During hydraulic fracturing in deep gas reservoirs, shale rocks may undergo extensive plastic deformation (Liu et al., 2019; Wang et al., 2024). This effect persists and propagates with fracture expansion. As hydraulic fractures advance, the original tip region undergoes ductile unloading, forming new plastic zones near the new tip due to stress concentration. Plastic strain accumulates around hydraulic fracture walls despite ductile unloading. To simulate shale formations under production conditions, both elastic–plastic formations during production and after fracturing must be described.

Many scholars have proposed models for calculating wellbore stress fields to describe plastic deformation during drilling (Wang et al., 2020; Xing et al., 2020; Zhang, 2020; Zhao et al., 2022). These models will be used to describe post-fracture deformation, simplifying it into plastic and elastic deformation models. The expressions for radial and tangential stresses of elastic and plastic deformation are as follows:

$$\begin{cases} \sigma_r^e = \sigma_h\left(1-\dfrac{R^2}{r^2}\right)+\dfrac{R^2}{r^2}\sigma_R+\dfrac{(1-2v)(p_w-p_{m0})}{2(1-v)}\left[1-\left(\dfrac{r_w}{r}\right)^2\right] \\ \sigma_\theta^e = \sigma_h\left(1+\dfrac{R^2}{r^2}\right)-\dfrac{R^2}{r^2}\sigma_R+\dfrac{(1-2v)(p_w-p_{m0})}{2(1-v)}\left[1+\left(\dfrac{r_w}{r}\right)^2\right] \end{cases} \tag{2}$$

$$\begin{cases} \sigma_r^p = p_w+\dfrac{p_{m0}-p_w}{\ln r_e-\ln r_w}\ln\dfrac{r_w}{r}-\dfrac{1}{\sqrt{3}}\dfrac{\sigma_c}{(e^{-1}-h)}\left(e^{-\frac{R^2}{r^2}}-e^{-\frac{R^2}{r_w{}^2}}+h\dfrac{r_w^2-r^2}{R^2}\right) \\ \sigma_\theta^p = p_w+\dfrac{p_{m0}-p_w}{\ln r_e-\ln r_w}\ln\dfrac{r_w}{r}-\dfrac{1}{\sqrt{3}}\dfrac{\sigma_c}{(e^{-1}-h)}\left(e^{-\frac{R^2}{r^2}}-e^{-\frac{R^2}{r_w{}^2}}+h\dfrac{r_w^2-3r^2}{R^2}+\dfrac{2R^2}{r^2}e^{-\frac{R^2}{r^2}}\right) \end{cases} \tag{3}$$

where $\sigma_r^e$ is the radial stress in the elastic zone, MPa; $\sigma_\theta^e$ is the tangential stress in the elastic zone, MPa; $\sigma_h$ is the far-field horizontal stress, MPa; $R$ is the radius of the plastic zone, m; $p_w$ is the bottom-hole pressure (BHP), MPa; $p_{m0}$ is the initial pressure of the formation, MPa; $r_w$ is the radius of the wellbore, m; $\sigma_R$ is the radial stress at the maximum radius of the plastic zone, MPa; $r$ is the distance from any point in the formation to the center of the wellbore, m; $\sigma_r^p$ is the radial stress in the plastic zone, MPa; $\sigma_\theta^p$ is the tangential stress in the plastic zone, MPa; $r_e$ is the supplying radius, m; $\sigma_c$ is the strength of the rock, MPa.

By incorporating Eqs. (2) and (3) as constraints into the initial stress conditions, the distribution of the elastic and elastoplastic formations after fracturing is simulated.

### 2.3. Governing equation of gas flow

A "dual-porosity dual-permeability" model for fractured horizontal wells is established to address the high pressure and low permeability of deep shale gas reservoirs. The mass conservation equations for the matrix region and the natural fracture are respectively expressed as follows:

$$\begin{cases} \dfrac{\partial m_{gm}}{\partial t}+\nabla\cdot\left(-\rho_g\dfrac{k_m k_{rgm}}{\mu_g}\nabla p_m\right)=-Q_{gmf} \\ \dfrac{\partial m_{wm}}{\partial t}+\nabla\cdot\left(-\rho_w\dfrac{k_m k_{rwm}}{\mu_w}\nabla p_m\right)=-Q_{wmf} \\ \dfrac{\partial m_{gf}}{\partial t}+\nabla\cdot\left(-\rho_g\dfrac{k_f k_{rgf}}{\mu_g}\nabla p_f\right)=Q_{gmf} \\ \dfrac{\partial m_{wf}}{\partial t}+\nabla\cdot\left(-\rho_w\dfrac{k_f k_{rwf}}{\mu_w}\nabla p_f\right)=Q_{wmf} \end{cases} \tag{4}$$

where $m_{gm}$ is the gas mass in the matrix, kg; $m_{gf}$ is the gas mass in the natural fractures, kg; $m_{wm}$ is the water mass in the matrix, kg; $m_{wf}$ is the water mass in the natural fractures, kg; $k_m$ is the permeability of the matrix, m$^2$; $k_f$ is the permeability of the natural fractures, m$^2$; $Q_{wmf}$ and $Q_{gmf}$ are the seepage between the matrix and natural fractures of water and gas, respectively, kg/s; $\rho_g$ is the gas density, kg/m$^3$; $\rho_w$ is the water density, kg/m$^3$; $k_{rgm}$ is the relative permeability of gas in the matrix; $k_{rgf}$ is the relative permeability of gas in the natural fractures; $k_{rwm}$ is the relative permeability of water in the matrix; $k_{rwf}$ is the relative permeability of water in the natural fractures; $p_m$ is the pressure of matrix; $p_f$ is the pressure of natural fracture.

This model considers free and adsorbed gas in the matrix, while only free gas is present in the natural fractures. Therefore, the gas mass in the shale matrix and natural fractures can be respectively represented as follows:

$$\begin{cases} m_{gm} = \rho_{gm}\phi_m S_{gm}+\dfrac{\rho_{ga}\rho_m V_L p_{gm}}{p_{gm}+p_L} \\ m_{wm} = \rho_{wm}\phi_m S_{wm} \\ m_{gf} = \rho_{gf}\phi_f S_{gf} \\ m_{wf} = \rho_{wf}\phi_f S_{wf} \end{cases} \tag{5}$$

where $\rho_{gm}$ and $\rho_{gf}$ respectively represent the shale gas density in the matrix and natural fractures, kg/m$^3$; $\phi_m$ and $\phi_f$ respectively represent the porosity of the matrix and natural fractures; $\rho_{ga}$ is the shale gas density at standard conditions, kg/m$^3$; $\rho_m$ is the shale

density, kg/m$^3$; $V_L$ is the Langmuir volume constant, m$^3$/kg; $S_{gm}$ is the gas saturation in the matrix; $S_{wm}$ is the water saturation in the matrix; $S_{gf}$ is the gas saturation in the natural fractures; $S_{wf}$ is the water saturation in the natural fractures.

The gas–water exchange term between the natural fractures and the matrix is given by

$$\begin{cases} Q_{gmf} = \rho_{gm} M_g k_m \alpha_g \left(p_{gm} - p_{gf}\right) \Big/ \left(RT_s Z_m \mu_g\right) \\ Q_{wmf} = \rho_{wm} k_m \alpha_w \left(p_{wm} - p_{wf}\right) \Big/ \mu_w \end{cases} \tag{6}$$

where $R$ is the universal gas constant, J/(mol·K); $M_g$ is the molar mass of the gas, kg/mol; $a_g$ and $a_w$ respectively represent inter-porosity flow coefficients of gas and water; $Z_m$ is the $Z$ factor in the matrix system; $T_s$ is the temperature of initial condition.

The formula for shale matrix permeability, considering simultaneously Knudsen diffusion, surface diffusion, adsorption–desorption, gas slip, and stress sensitivity, can be expressed as follows:

$$k_{m1} = \frac{1+F}{m} k_{m0} \left[ \left(1 + \frac{\mu_m D_{km}}{p_m k_{m0}}\right) + k_{sf} \right] \tag{7}$$

where $k_{m0}$ is the initial matrix permeability, m$^2$; $k_{sf}$ is the apparent permeability of the shale matrix characterized by surface diffusion, m$^2$; $D_{km}$ is the diffusion coefficient in the matrix; $F$ is the slippage correction factor; $m$ is the stress sensitivity coefficient.

### 2.4. Dynamic coupling equations

A dynamic coupling model considering post-fracturing rock plastic deformation and multi-scale transport mechanisms is established by dynamically coupling effective stress with permeability and porosity.

#### 2.4.1. Dynamic porosity and permeability of matrix

According to previous studies (Cao et al., 2016b; Wang et al., 2018), the dynamic porosity model for the matrix can be expressed as follows:

$$\phi_m = \frac{(1+M_0)\phi_{m0} + \alpha(M - M_0)}{1+M} \tag{8}$$

with

$$M = \varepsilon_{kk} + \frac{\left(S_{gm} p_{gm} + S_{wm} p_{wm}\right)}{K_s} - \varepsilon_s$$

$$M_0 = \varepsilon_{kk0} + \frac{\left(S_{gm0} p_{gm0} + S_{wm0} p_{wm0}\right)}{K_s} - \varepsilon_{s0}$$

$$\varepsilon_{kk} = \frac{\overline{\sigma_m}}{K_m} + \varepsilon_s$$

$$\overline{\sigma_m} = \frac{1}{3}\sigma_{kk} + \alpha\left(S_{gm} p_{gm} + S_{wm} p_{wm}\right)$$

$$\sigma_{kk} = \left(\sigma_\theta^p + \sigma_r^p + \sigma_c\right)/3$$

where $\varepsilon_{s0}$ is the initial adsorption strain; $\varepsilon_{kk0}$ is the initial volume strain of the shale; $\varepsilon_{kk}$ is the volume strain of shale; $\overline{\sigma_m}$ is the effective stress within the matrix; $\sigma_{kk}$ is the volume stress; $\sigma_\theta^p$ is the tangential stress (plastic); $\sigma_r^p$ is the radial stress (plastic).

Based on the numerous permeability models, the Kozeny–Carman equation is the most widely used permeability model (Xu and Yu, 2008). The coupled permeability of shale matrix, considering Knudsen diffusion, surface diffusion, adsorption–desorption, gas slip, stress sensitivity, and rock elastoplastic deformation, can be expressed as follows:

$$k_m = \frac{1+F}{m} k_{m0} \left[ \left(1 + \frac{\mu_m D_{km}}{p_m k_{m0}}\right) + k_{sf} \right] \left(\frac{\phi_m}{\phi_{m0}}\right)^3 \tag{9}$$

#### 2.4.2. Dynamic porosity and permeability of natural fracture

Compression and matrix deformation cause changes in the aperture of natural fractures, thereby altering the porosity and original permeability of the natural fractures. According to scholars' research, the porosity model for natural fractures can be expressed as follows (Zhao et al., 2020):

$$\phi_f = \phi_{f0} \exp\left[ \frac{\overline{\sigma_f} - \overline{\sigma_{f0}}}{K_p} - \frac{\overline{\sigma_m} - \overline{\sigma_{m0}}}{K_m} - \left(\varepsilon_s - \varepsilon_{s0}\right) \right] \tag{10}$$

with

$$\overline{\sigma_f} = \frac{1}{3}\sigma_{kk} + \beta\left(S_{gf} p_{gf} + S_{wf} p_{wf}\right)$$

where $\overline{\sigma_{f0}}$ is the initial effective stress in natural fractures; $\overline{\sigma_{m0}}$ is the initial effective stress in the matrix; $\overline{\sigma_f}$ is the effective stress within the natural fracture. According to the cubic relationship between natural fracture porosity and permeability (Wu et al., 2011), the dynamic permeability model for natural fractures is

$$k_f = k_{f0} \frac{1+F}{m} \exp\left\{ 3\left[ \frac{\overline{\sigma_f} - \overline{\sigma_{f0}}}{K_p} - \frac{\overline{\sigma_m} - \overline{\sigma_{m0}}}{K_m} - \left(\varepsilon_s - \varepsilon_{s0}\right) \right] \right\} \tag{11}$$

where $k_{f0}$ is the initial permeability of shale natural fractures.

The above dynamic coupling equations between shale deformation and gas flow, combined with the governing equations of plastic deformation and gas flow, form a fully coupled multi-physics model.

## 3. Model implementation and validation

In this section, the finite element method will be used to solve the established coupled flow and geomechanics model. The accuracy of the model will be verified by the classic mechanical Mandel problem (Mandel, 1953) and practical applications.

### 3.1. Model validation

The physical model is a rectangular porous elastic medium filled with fluid, sandwiched between two frictionless rigid plates.

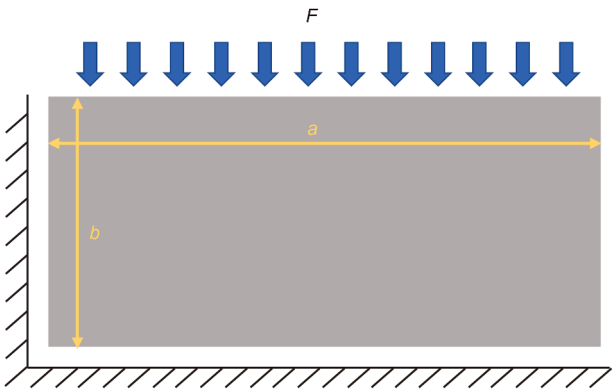


**Fig. 4.** Schematic diagram of the Mandel problem model.

The sides are drained with no traction and an instantaneous force acts on the top surface. The geometric model of the Mandel problem is shown in Fig. 4. A numerical model is constructed using parameters in Table 1. Due to symmetry in structure and loading, only a quarter of the domain is generated. Goulet et al. (2009) provided the analytical solution for pore pressure. The calculated pore pressure on the top interface is compared with the analytical solution in Fig. 5, showing good agreement and confirming the model's accuracy.

### 3.2. Practical applications

Well Y1 is a deep shale gas well in the Sichuan Basin at a depth of 3845 m. The porosity ranges from 2.1% to 9.6%, averaging 5.5%. The matrix porosity averages between 4.6% and 5.4%. Permeability ranges from 0.01 to 0.20 mD, averaging 0.06 mD. Gas content ranges from 3.3 to 8.5 $m^3$/t, averaging 5.5 $m^3$/t. Table 2 shows the reservoir and fracturing parameters.

Based on the daily and cumulative gas production curves of Well Y1 (Figs. 6 and 7), the model's fit closely matches the actual production dynamics during normal operation. The high overall fitting accuracy indicates good model performance. Compared to the elastic model, the elastoplastic model aligns with the actual production of Well Y1, demonstrating its applicability to real production wells.

## 4. Results and discussion

In this section, the impact of the elastoplastic model on the permeability of the matrix and natural fractures is compared in deep shale gas reservoirs. Then, the effects of various parameters are discussed on production, then the principal factors are obtained.

**Table 1**
Calculation parameters for the Mandel problem.

| Parameter | Value |
|---|---|
| Biot coefficient | 0.93 |
| Poisson's ratio | 0.2 |
| Young's modulus, GPa | 15 |
| Fluid compressibility modulus, MPa | 3000 |
| Porosity | 0.1 |
| Permeability, mD | 100 |

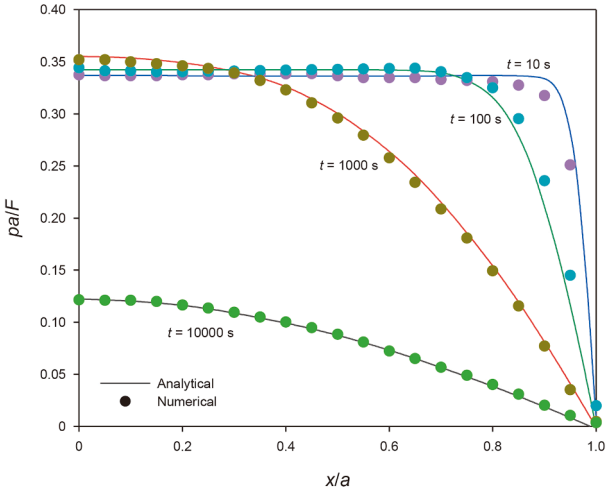


**Fig. 5.** Comparison of numerical simulation results with analytical solution.

### 4.1. Model implementation

This section is to establish a dynamic numerical model simulating the production of deep hydraulically fractured horizontal wells considering shale elastoplastic deformation. The model is symmetric around the wellbore. The geometry of the two-dimensional model is illustrated in Fig. 8. The dimensions of the model are 500 m horizontally and 150 m vertically. The total length of the horizontal well is 400 m with a half-fracture length of 90 m. There are four hydraulic fractures, spaced 100 m apart. The reservoir is initially at a uniform pressure, the model is subjected to an initial pore pressure of 50 MPa, with constant pressure production at a flowing bottom-hole pressure of 30 MPa. The left, right, and top boundaries are mechanically constrained with zero normal displacement, representing impermeable and rigid boundaries. The entire model is treated as elastoplastic material. Material properties for the baseline case are listed in Table 3. The relative permeability curves of the matrix and natural fractures are

**Table 2**
Basic reservoir parameters.

| Parameter | Value | Parameter | Value |
|---|---|---|---|
| Reservoir pressure, MPa | 90 | Gas density, kg/$m^3$ | 0.4 |
| Formation temperature, K | 408.15 | Gas molar mass, kg/mol | 0.0195 |
| Fracture length, m | 80 | Fracture width, m | 0.003 |
| Horizontal well length, m | 1500 | Horizontal well spacing, m | 300 |
| Number of fracture stages | 20 | BHP, MPa | 20 |
| Reservoir thickness, m | 37 | Wellbore radius, m | 0.1 |
| Matrix porosity, % | 5.5 | Depth, m | 3845 |

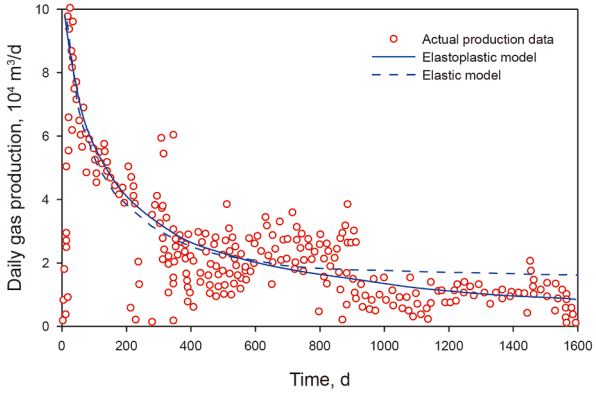


**Fig. 6.** Comparison of model results against the daily production history.

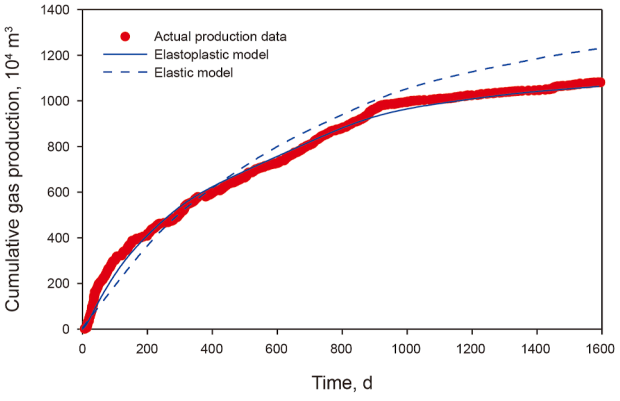


**Fig. 7.** Comparison of model results against the cumulative production history.

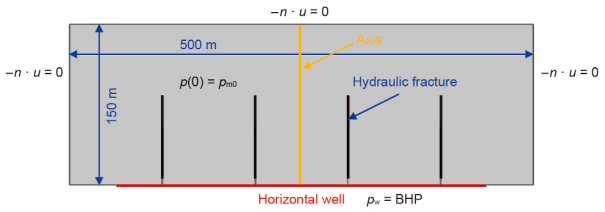


**Fig. 8.** Numerical model considering elastoplastic deformation.

elastic formations increases with distance and decreases with time, while in the elastoplastic formations, the $k_m/k_0$ decreases and then increases with distance, and decreases with time. The minimum $k_m/k_0$ value shifts 25 m outward from 100 to 1000 d. The permeability ratio in elastic formations is always higher than in plastic formations. Fig. 13 shows that the microfracuture permeability has a similar pattern, but the minimum $k_f/k_0$ value shifting 10 m from 300 to 1000 d.

Due to the plasticity of the formation, its permeability is

**Table 3**
Input parameters for basic simulation analysis.

| Parameter | Value | Parameter | Value |
|---|---|---|---|
| Initial matrix porosity $\phi_{m0}$ | 0.00935 | Initial fracture porosity $\phi_{f0}$ | 0.0624 |
| Initial matrix permeability $k_{m0}$, mD | 0.00002 | Stress sensitivity $m$ | 0.1 |
| Slip correction coefficient $F$ | 1.017 | Initial temperature $T_s$, K | 485 |
| Langmuir volume constant $V_L$, $m^3$/kg | 0.00272 | Langmuir pressure $p_L$, MPa | 4.48 |
| Critical pressure $p_c$, MPa | 4.64 | Critical temperature $T_c$, K | 191.05 |
| Initial pressure $p_{m0}$, MPa | 50 | BHP $p_w$, MPa | 30 |
| Gas constant $R$, J/(mol·K) | 8.314 | Gas molar mass $M_g$, kg/mol | 0.016 |
| Natural fracture aperture $b$, mm | 0.009 | Natural fracture spacing $s$, m | 0.5 |
| Hydraulic fracture aperture $d_f$, m | 0.005 | Rock density $\rho_m$, kg/$m^3$ | 2600 |
| Water viscosity $\mu_w$, mPa·s | 1.0 | Water density $\rho_w$, kg/$m^3$ | 1000 |
| Initial water saturation in the matrix $S_{wm}$ | 0.25 | Initial water saturation in the fracture $S_{wf}$ | 0.55 |
| Young's modulus $E$, GPa | 1.3 | Poisson's ratio $v$ | 0.15 |
| Rock strength $\sigma_c$, MPa | 15 | Langmuir strain constant $\varepsilon_L$ | 0.02295 |

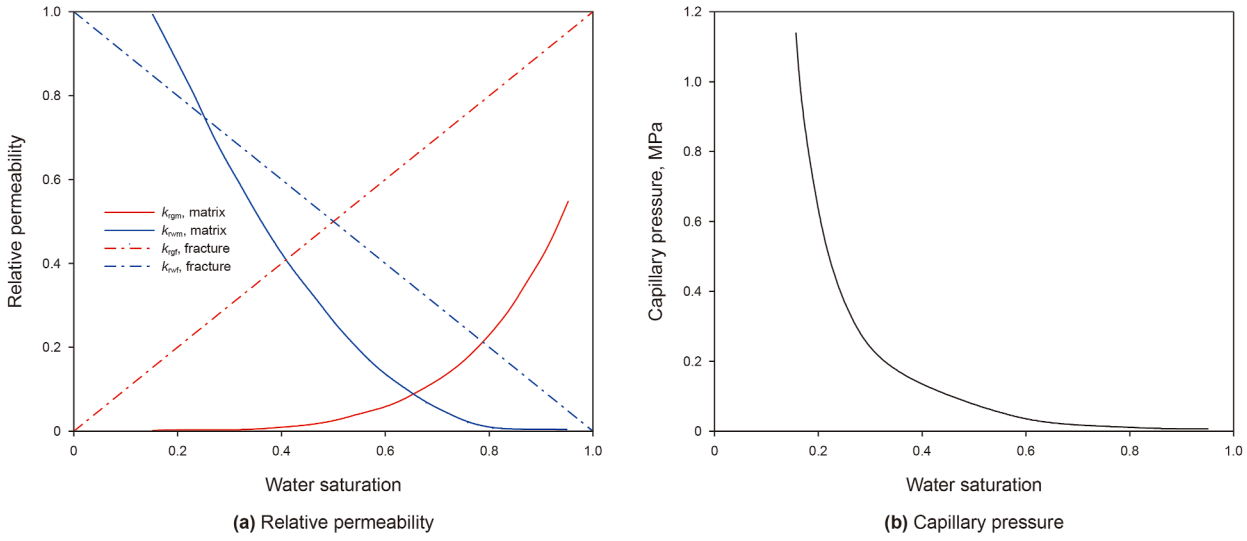


**(a)** Relative permeability **(b)** Capillary pressure

**Fig. 9.** Curves of relative permeability and capillary pressure.

shown in Fig. 9(a), and the capillary pressure curve of the matrix is shown in Fig. 9(b).

### 4.2. Comparison of elastic and elastoplastic models

The matrix and natural fracture permeability plot with BHP of 25 MPa are shown in Figs. 10 and 11. As shale gas is continuously developed, reservoir pressure gradually decreases. This causes pore and natural fracture closure in the near-well zone, reducing matrix and natural fracture permeability, while the matrix and natural fracture permeability of the elastic formation is higher than that of the elastoplastic formation at 25 MPa.

The matrix and natural fracture permeability variation curves are shown in Figs. 12 and 13. In Fig. 12, the value of $k_m/k_0$ in the

influenced by the deformation of the formation and the pore structure. During the depletion-type exploitation of the formation, the deformation of the formation leads to the evolution of pores and natural fractures. Initially, stress changes during fracturing cause contraction or closure, temporarily decreasing permeability. Over time, the formation adapts and pore structure readjusts, increasing permeability. In which due to formation non-uniformity, the near-well zone is more susceptible to external influences with more natural fractures and pores. This causes delayed production impact away from the wellbore, shifting the minimum value outward. Matrix permeability is more sensitive to external pressure than natural fracture permeability, leading to an earlier shift of the minimum value towards the far-well zone.

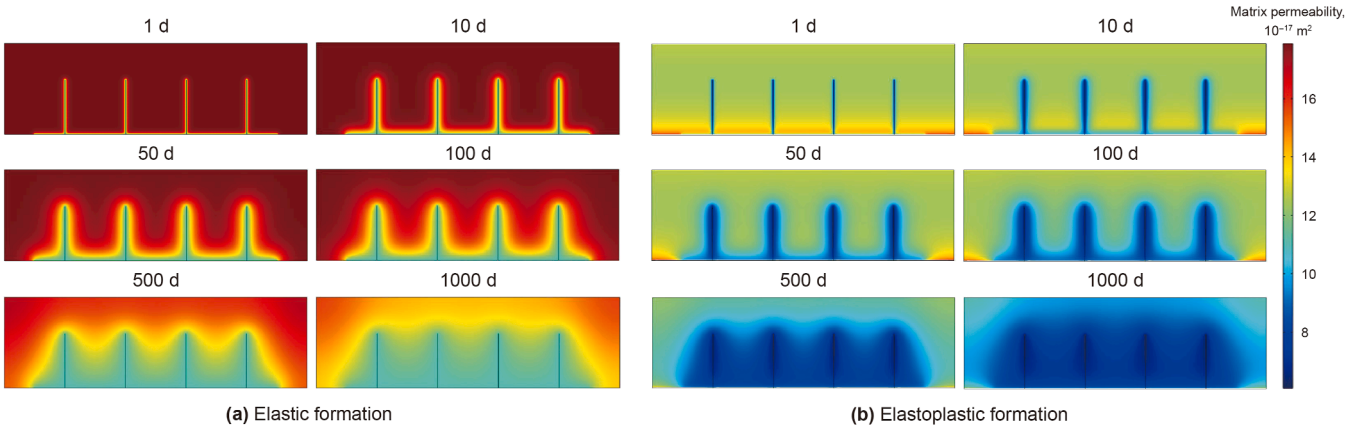


**Fig. 10.** Matrix permeability distribution at different times.

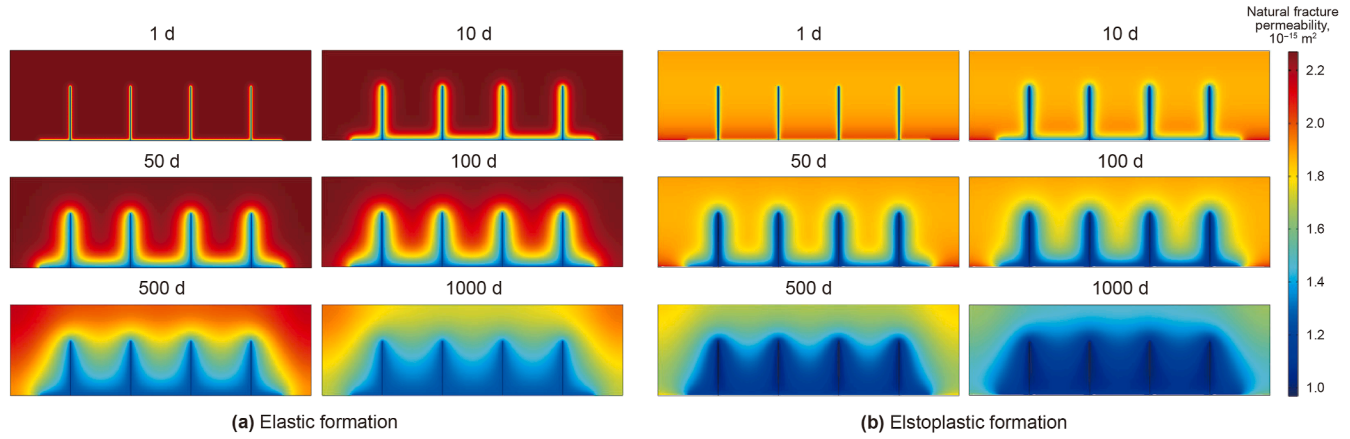


**Fig. 11.** Natural fracture permeability distribution at different times.

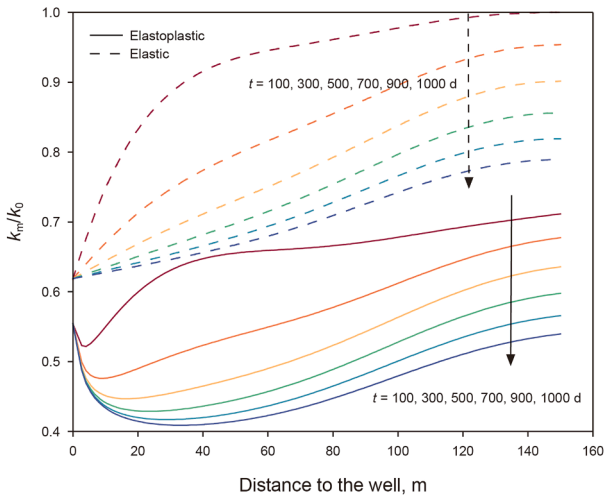


**Fig. 12.** Matrix permeability variations over time and distance.

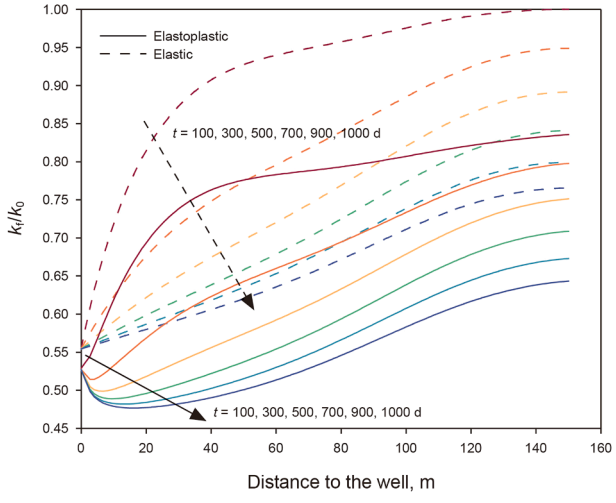


**Fig. 13.** Natural fracture permeability variations over time and distance.

### 4.3. Effect of elastoplastic deformation on production

The production rate and cumulative production variations of elastic and elastoplastic formations under different BHP is shown in Fig. 14. In Fig. 14(a), as the time increases in the elastic formation, the production rate decreases and the cumulative production increases. Both curves decline with increasing BHP. In Fig. 14(b), as the time increases in the elastoplastic formation, the daily production decreases and the cumulative production increases. However, both curves first rise and then fall with

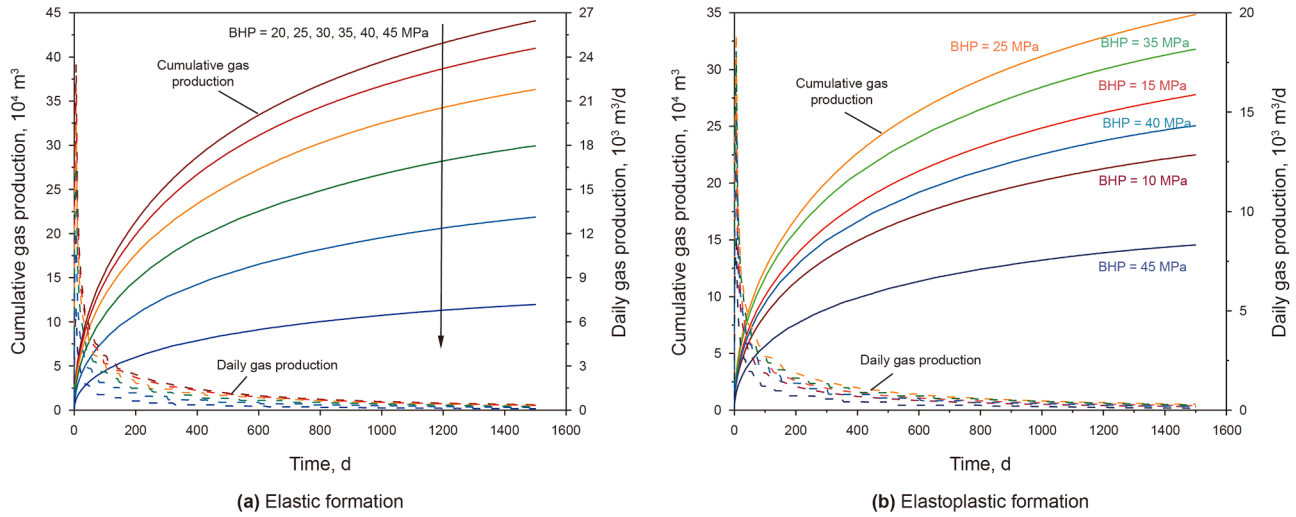


**Fig. 14.** Daily and cumulative gas production under different BHP.

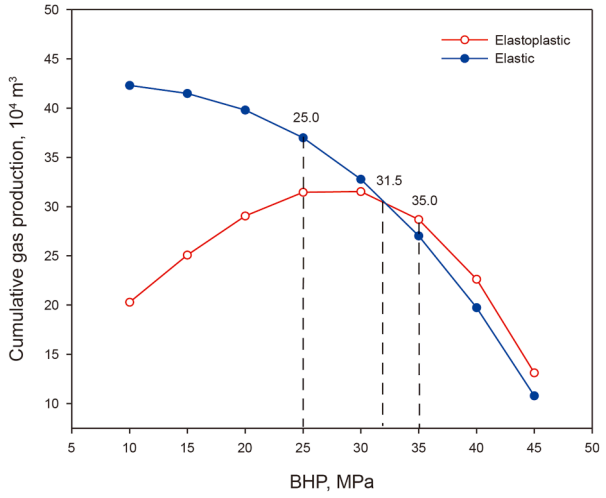


**Fig. 15.** Cumulative gas production of elastic and elastoplastic formations under different BHP.

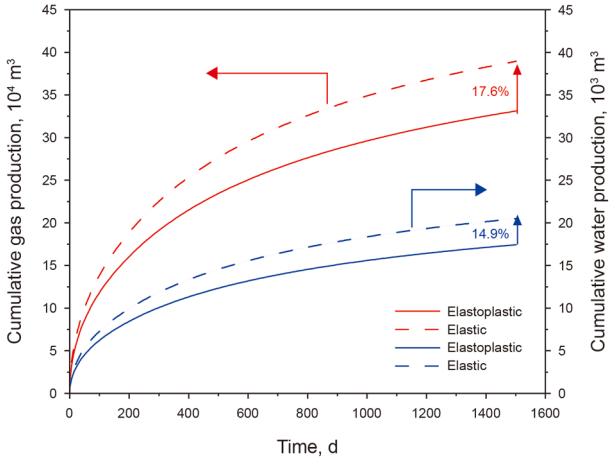


**Fig. 16.** Cumulative gas and water production of elastic and plastic formations.

increasing BHP. Cumulative production changes under BHP are shown in Fig. 15.

As shown in Fig. 15, the production of elastoplastic formations reaches its maximum around BHP of 31.5 MPa. Additionally, when the pressure is below 31.5 MPa, the production of elastic formations is higher than that of elastoplastic formations; while when the pressure exceeds 31.5 MPa, the production of elastic formations is lower than that of elastoplastic formations. Fig. 16 illustrates that, at a BHP of 25 MPa, the cumulative gas and water production in the elastic model exceed those in the elastoplastic model. The gas production is higher by 17.6%, and the water production is higher by 14.9%.

With constant original formation pressure, a decrease in flow pressure increases the production pressure differential, enhancing shale gas flow and recovery rate. In elastic formations, production increases as the flow pressure decreases. But in elastoplastic formation, higher pressure differentials cause plastic deformation, reducing pore channels and fluid movement, decreasing production. To prevent the closure of pore and natural fracture channels, determining a reasonable production pressure differential is crucial for the development of deep shale gas reservoirs.

This study presents the dynamic characteristics of matrix and natural fracture permeability variations with time and distance from the well under different BHP (25, 31.5, and 45 MPa) in Figs. 12, 13 and 17. The results reveal that the evolution of permeability is jointly influenced by pressure conditions and temporal factors. As shown in Figs. 12, 13 and 17, both matrix permeability and natural fracture permeability exhibit an initial decrease followed by an increase with distance in the elastoplastic model, whereas the elastic model shows a gradual increase with distance. Over time, the permeability of all models decreases. At a BHP of 25 MPa, the elastic model demonstrates higher permeability than the elastoplastic model. When the BHP increases to 31.5 MPa, the permeability values of the elastic and elastoplastic models become comparable. However, at 45 MPa, the elastoplastic model exhibits higher permeability than the elastic model.

Cumulative production of elastic and elastoplastic formations with different times is shown in Fig. 18. The positions of the elastoplastic extremum and the crossover point remain constant and are independent of the production time. Therefore, subsequent analyses will be based on cumulative production results at 1500 d.

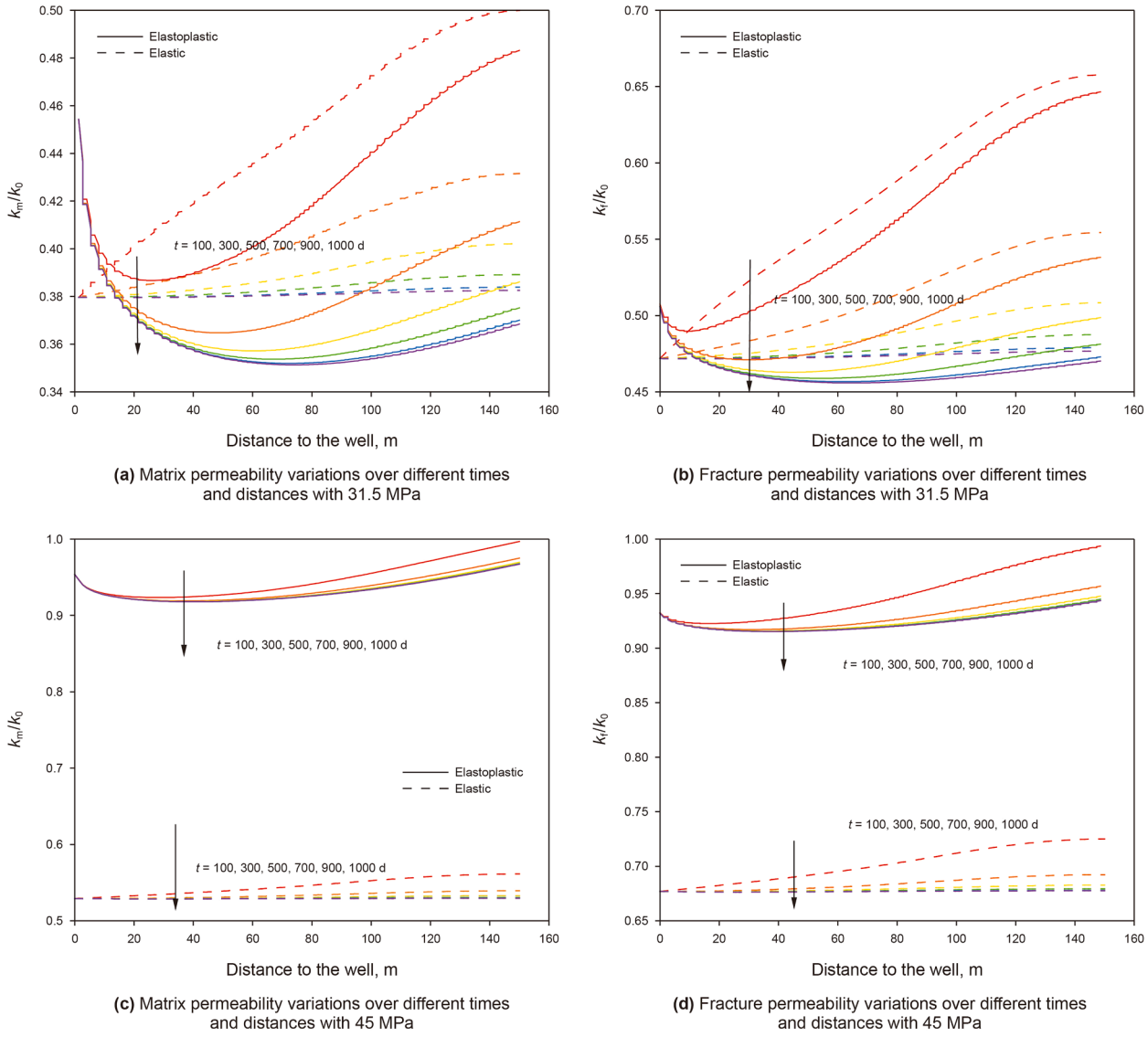


**Fig. 17.** Matrix and natural fracture permeability variations over time and distance.

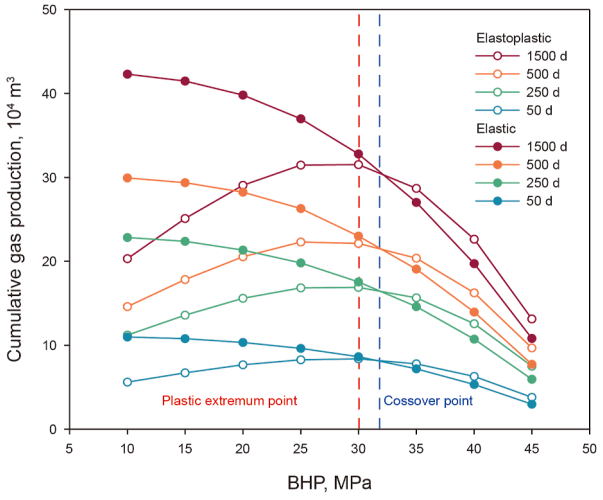


**Fig. 18.** Cumulative gas production of elastic and elastoplastic formations over time.

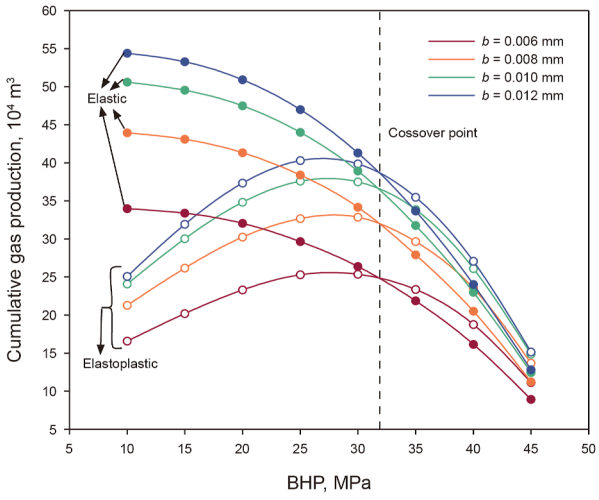


**Fig. 19.** Cumulative gas production under different natural fracture apertures.

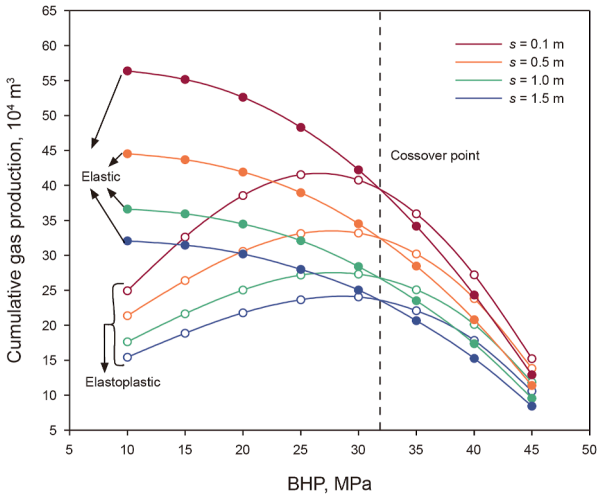


**Fig. 20.** Cumulative gas production under different natural fracture spacing.

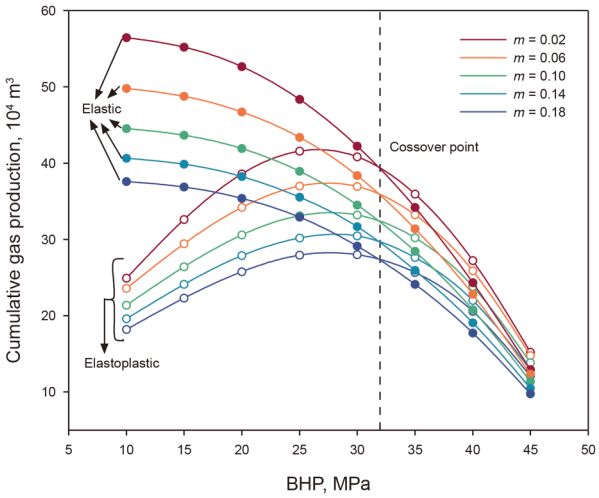


**Fig. 22.** Cumulative gas production under different stress sensitivity parameters.

### 4.4. Effect of model parameters on production

In this section, we examine the influence of various parameters on deep shale gas production. Each parameter is changed individually while others remain constant, as summarized in Table 3. The parameters examined include natural fracture aperture, natural fracture spacing, initial matrix permeability, stress sensitivity, Poisson's ratio, and original reservoir pressure.

#### 4.4.1. Natural fracture aperture

The cumulative production of elastic and elastoplastic formations is presented in Fig. 19 as a function of BHP under various natural fracture apertures. As the aperture increases from 0.006 to 0.012 mm, the rate of cumulative production growth slows in both models. The intersection point between elastic and elastoplastic production remains constant at 31.5 MPa. Maximum elastoplastic production occurs at 25 and 30 MPa. Overall, when BHP < 31.5 MPa, elastic formations yield 52.30% more production than elastoplastic ones. Therefore, for elastic formations, maintaining BHP below 31.5 MPa results in higher production. Conversely, when BHP > 31.5 MPa, elastoplastic formations yield 21.10% more production than elastic ones, indicating that after the formation undergoes elastoplastic deformation, BHP above 31.5 MPa leads to increased production.

#### 4.4.2. Natural fracture spacing

Fig. 20 shows the cumulative production over 1500 d versus BHP for different natural fracture spacing. As the spacing increases from 0.1 to 1.5 m, the production from both elastic and elastoplastic formations declines, but at a diminishing rate. The intersection point remains at 31.5 MPa, unaffected by natural fracture spacing. Peak elastoplastic production occurs at 25 and 30 MPa. When BHP < 31.5 MPa, elastic formations produce 52.88% more than elastoplastic ones. When BHP > 31.5 MPa, elastoplastic formations produce 22.21% more than elastic ones. This suggests that for elastic formations, BHP should be kept below 31.5 MPa for higher production, whereas after elastoplastic deformation, BHP above 31.5 MPa enhances production.

#### 4.4.3. Initial matrix permeability

Fig. 21 shows the cumulative production over 1500 d versus BHP for different initial matrix permeability. As the permeability increases, both elastic and elastoplastic production rise at an accelerating rate. The intersection point remains unchanged

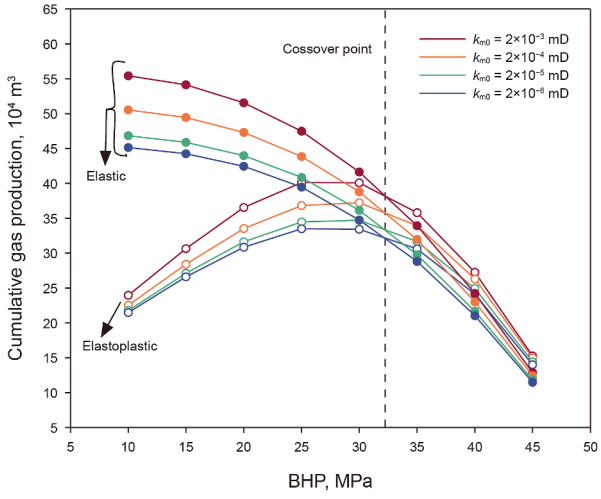


**Fig. 21.** Cumulative gas production under different initial matrix permeability.

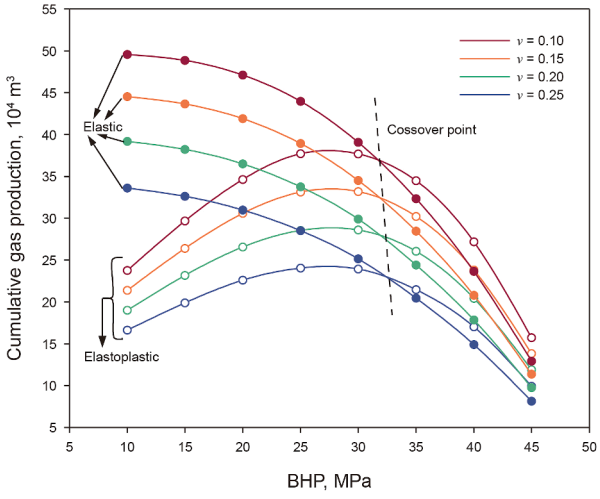


**Fig. 23.** Cumulative gas production under different Poisson's ratios.

despite permeability variations. When BHP < 31.5 MPa, elastic formations yield about 53.96% more than elastoplastic ones. When BHP > 31.5 MPa, elastoplastic formations yield about 20.81% more than elastic ones. It indicates that maintaining BHP below 31.5 MPa optimizes production in elastic formations, while after elastoplastic deformation, BHP above 31.5 MPa yields higher production.

#### 4.4.4. Stress sensitivity parameter

Fig. 22 shows the cumulative production of elastic and elastoplastic formations versus BHP for different stress sensitivity parameters. As the stress sensitivity parameter increases from 0.02 to 0.18, the cumulative production decreases in both models. Peak elastoplastic production occurs at 25 and 30 MPa. When BHP < 31.5 MPa, elastic formations yield about 52.77% more than elastoplastic ones. When BHP > 31.5 MPa, elastoplastic formations yield about 21.14% more than elastic ones. For elastic formations, keeping BHP below 31.5 MPa maximizes production, while after elastoplastic deformation, exceeding 31.5 MPa enhances output.

#### 4.4.5. Poisson's ratio

Fig. 23 shows the cumulative production over 1500 d versus BHP for different values of Poisson's ratio. As Poisson's ratio increases from 0.10 to 0.25, the cumulative production decreases in both elastic and elastoplastic models. The intersection point shifts along the line $y = -161315.5x + 5509460.2$, showing Poisson's ratio affects its lateral movement. Maintaining elastoplastic reservoir BHP between 25 and 30 MPa leads to higher production. Below the line $y$, elastic formations yield 51.53% more than elastoplastic ones, above the line $y$, elastoplastic formations yield 21.75% more than elastic ones. For elastic formations, BHP should be left of the line $y$, whereas after elastoplastic deformation, it should be right of the line $y$.

#### 4.4.6. Original reservoir pressure

Fig. 24 shows the cumulative production over 1500 d versus BHP for different initial reservoir pressures. As the original reservoir pressure increases from 30 to 70 MPa, the cumulative production increases in both elastic and elastoplastic models. The intersection point of elastic and elastoplastic production shifts along the line $y = 5052.3x - 876399.9$, indicating the impact of original reservoir pressure on its lateral movement. For elastic formations, BHP should be left of the line $y$, whereas after elastoplastic deformation, it should be right of the line $y$. To sum up, the initial reservoir pressure plays a crucial role in determining the production preference between elastic and elastoplastic formations.

The elastoplastic peak noticeably shifts rightward as the reservoir pressure rises. At an original reservoir pressure of 30 MPa, the elastoplastic peak aligns with a BHP of 15 MPa. This trend continues as the original reservoir pressure increases to 70 MPa, shifting the elastoplastic peak to a BHP of 40 MPa. This highlights the critical role of reservoir pressure in determining the elastoplastic peak's position. To optimize production, maintaining BHP between 0.5 and 0.625 times the original reservoir pressure for elastoplastic formations across different reservoir pressures is essential.

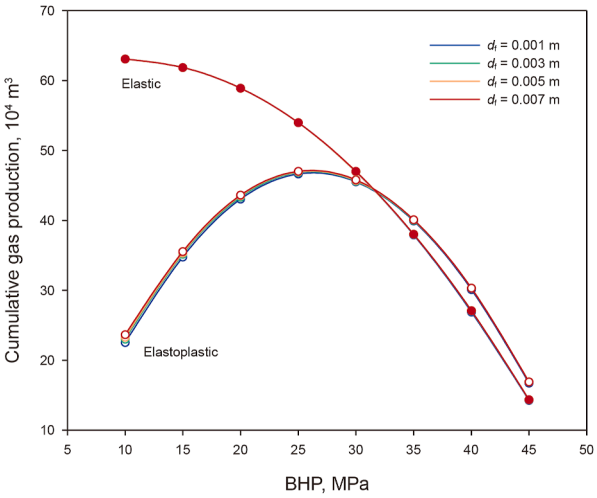


**Fig. 25.** Cumulative gas production under different hydraulic fracture apertures.

#### 4.4.7. Hydraulic fracture aperture

Fig. 25 shows the variation in cumulative production over 1500 d with BHP for different hydraulic fracture apertures. As the hydraulic fracture aperture increases, both elastic and elastoplastic production increase, but the increment is relatively small and the change is not significant. Despite the variation in aperture, the intersection point remains unchanged.

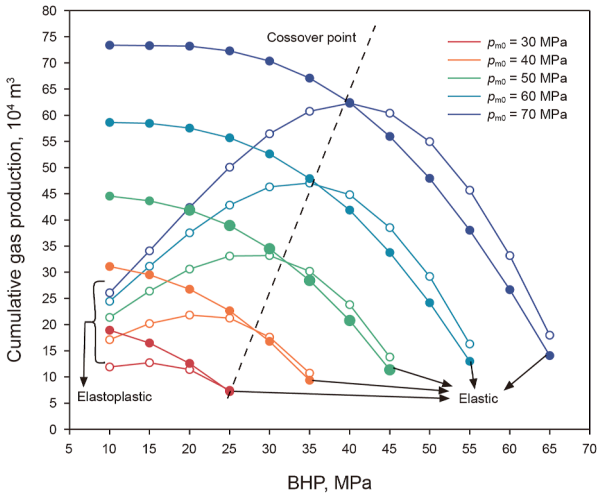


**Fig. 24.** Cumulative gas production under different initial reservoir pressures.

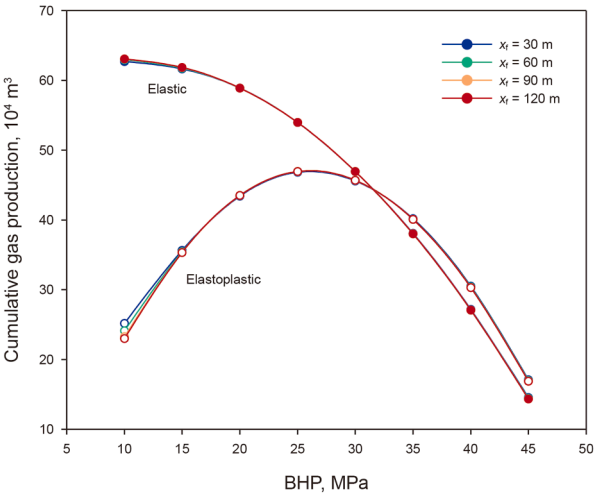


**Fig. 26.** Cumulative gas production under different hydraulic fracture half-lengths.

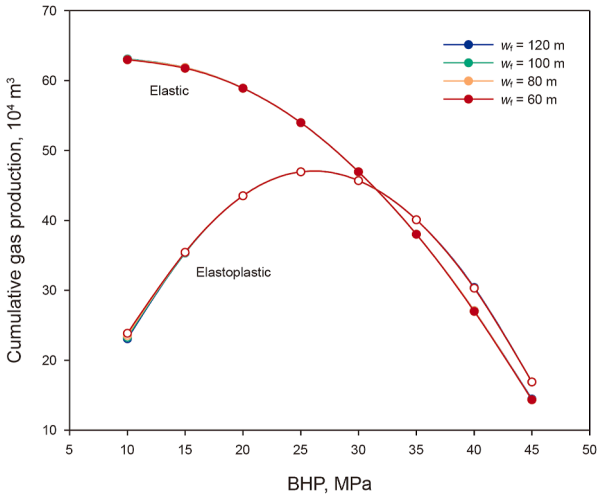


**Fig. 27.** Cumulative production under different hydraulic fracture spacing.

When BHP < 31.5 MPa, the elastic formation exhibits approximately 64.32% higher production than the elastoplastic formation. Conversely, when BHP > 31.5 MPa, the elastoplastic formation yields about 14.94% higher production than the elastic formation. This indicates that maintaining BHP below 31.5 MPa enhances production in elastic formations, whereas keeping BHP above 31.5 MPa after elastoplastic deformation occurs leads to higher production.

#### 4.4.8. Hydraulic fracture half-length

Fig. 26 illustrates the variation in 1500-d cumulative production under different hydraulic fracture half-lengths. As the hydraulic fracture half-length increases, production decreases slightly in both elastic and elastoplastic formations, though the reduction is marginal and shows no significant variation. Notably, the intersection point remains constant despite changes in fracture half-length. When BHP < 31.5 MPa, the elastic formation demonstrates approximately 59.85% higher production than the elastoplastic formation. Conversely, when BHP > 31.5 MPa, the elastoplastic formation yields about 15.09% greater production than the elastic formation.

#### 4.4.9. Hydraulic fracture spacing

Fig. 27 demonstrates the variation of 1500-d cumulative production with BHP under different hydraulic fracture spacing. The results show that as the fracture spacing increases, production in both elastic and elastoplastic formations exhibits a slight upward trend, though the increment remains relatively minor with no significant variation. Remarkably, the intersection point maintains its position despite changes in fracture spacing. When BHP < 31.5 MPa, elastic formations outperform elastoplastic formations by approximately 63.36% in production. Conversely, when BHP > 31.5 MPa, elastoplastic formations show about 15.02% higher production than elastic formations.

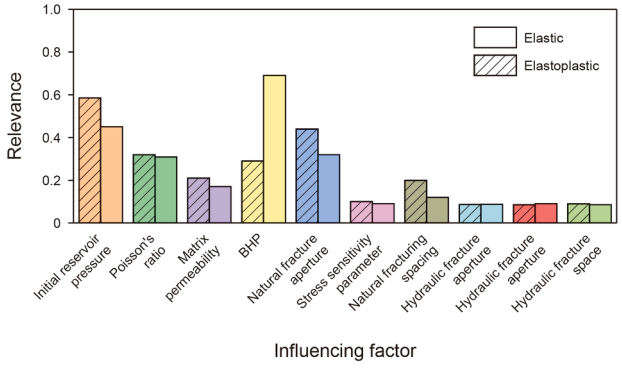


**Fig. 28.** Influence of different factors on elastic and elastoplastic production.

### 4.5. Analysis of principal factors

The production of deep shale gas from fractured horizontal wells is influenced by various factors, with differing impacts on elastic and elastoplastic formations. To analyze the main factors, variables such as BHP, initial reservoir pressure, Poisson's ratio, initial matrix permeability, stress sensitivity, natural fracture spacing, and aperture are considered, using cumulative gas production over 1500 d to determine primary and secondary relationships, as shown in Fig. 28.

Results show that among all factors, initial reservoir pressure has the greatest impact on elastoplastic formation production, followed by natural fracture spacing. BHP has the greatest impact on elastic formation production, followed by initial reservoir pressure. Thus, the main factors affecting deep shale gas production are initial reservoir pressure, BHP, and natural fracture spacing.

## 5. Conclusions

This paper establishes a fully coupled model for hydraulic fracturing in deep shale gas reservoirs, considering post-fracturing elastoplastic deformation. It describes production performance with flow-geomechanics coupling. Through analysis, the following conclusions are drawn:

(1) The initial fracturing of the formation leads to a temporary contraction, resulting in a decrease in permeability. However, subsequent pore structure readjustment during production causes an increase in permeability. Formation heterogeneity leads to varied production responses across regions, with areas distant from the well responding more slowly, causing the minimum permeability to shift right over time.

(2) As the bottom-hole pressure (BHP) increases, the elastic production decreases, while elastoplastic production initially increases and then decreases. The temporal aspect of production does not exert an influence on the position of the elastoplastic maximum point or the intersection point between elastic and elastoplastic production.

(3) When the initial reservoir pressure is 50 MPa and the BHP is less than 31.5 MPa, elastic exploitation is preferable; when the BHP exceeds 31.5 MPa, elastoplastic exploitation is preferable.

(4) Poisson's ratio and original formation pressure mainly affect the elastic and elastoplastic intersection point. The initial reservoir pressure determines the optimal range of BHP for elastoplastic formations, ideally 0.5 to 0.625 times the original formation pressure for higher production.

(5) Among the influencing factors, initial reservoir pressure has the greatest impact on elastoplastic formation production, followed by natural fracture spacing. BHP has the greatest influence on elastic formation production, followed by original formation pressure.

## CRediT authorship contribution statement

**Dong-Yan Fan:** Writing – review & editing, Supervision, Resources, Funding acquisition. **Can Yang:** Writing – review & editing, Writing – original draft, Visualization, Validation, Investigation. **Hai Sun:** Supervision, Project administration, Funding acquisition. **Jun Yao:** Supervision, Methodology, Funding acquisition. **Xia Yan:** Supervision, Software, Resources. **Lei Zhang:** Methodology, Funding acquisition, Conceptualization. **Cun-Qi Jia:** Supervision, Funding acquisition. **Gloire Imani:** Project administration. **Si-Cen Lai:** Formal analysis. **Liang Zhou:** Conceptualization.

## Conflict of interest

We declare that we have no financial and personal relationships with other people or organizations that can inappropriately influence our work, there is no professional or other personal interest of any nature or kind in any product, service and/or company.

## Acknowledgments

We would like to express appreciation to the National Natural Science Foundation of China (Grant Nos. U24B6001, 42090024), National Science and Technology Major Project (Grant No.2025ZD1404106) and Shandong Provincial Natural Science Foundation (Grant No. ZR2022JQ23).

## Appendix A. Supplementary data

Supplementary data to this article can be found online at https://doi.org/10.1016/j.petsci.2025.10.005.

## References

Bai, J., Wang, X.Q., Ge, H.K., Meng, H., Wen, Y.Q., 2023. Effect of hydraulic fracturing induced stress field on weak surface activation during unconventional reservoir development. Pet. Sci. 20 (5), 3119–3130. https://doi.org/10.1016/j.petsci.2023.05.003.

Biot, M.A., 1941. General theory of three-dimensional consolidation. J. Appl. Phys. 12 (2), 155–164. https://doi.org/10.1063/1.1712886.

Biot, M.A., 1955. Theory of elasticity and consolidation for a porous anisotropic solid. J. Appl. Phys. 26 (2), 182–185. https://doi.org/10.1063/1.1721956.

Cao, P., Liu, J.S., Leong, Y.K., 2016a. A fully coupled multiscale shale deformation-gas transport model for the evaluation of shale gas extraction. Fuel 178, 103–117. https://doi.org/10.1016/j.fuel.2016.03.055.

Cao, P., Liu, J.S., Leong, Y.K., 2016b. Combined impact of flow regimes and effective stress on the evolution of shale apparent permeability. Journal of Unconventional Oil and Gas Resources 14, 32–43. https://doi.org/10.1016/j.juogr.2016.01.004.

Goulet, G., Cooper, D.M.L., Coombe, D., Zernicke, R.F., 2009. Validation and application of iterative coupling to poroelastic problems in bone fluid flow. Bulletin of Applied Mechanics 5, 6–16.

Guo, L., Wang, Z., Zhang, Y., Wang, Z., Jiang, H., 2020. Experimental and numerical evaluation of hydraulic fracturing under high temperature and embedded fractures in large concrete samples. Water 12 (11), 3171. https://doi.org/10.3390/w12113171.

Hu, X.L., Li, K.Q., Qu, S.J., 2019. The elastoplastic constitutive model of rock and its numerical implementation based on unified strength theory. Explos. Shock Waves 39 (8), 083108. https://www.bzycj.cn/cn/article/doi/10.11883/bzycj-2019-0044 (in Chinese).

Hu, Y., Liu, G., Luo, N., Gao, F., Yue, F., Gao, T., 2022. Multi-field coupling deformation of rock and multi-scale flow of gas in shale gas extraction. Energy 238, 121666. https://doi.org/10.1016/j.energy.2021.121666.

Javadpour, F., 2009. Nanopores and apparent permeability of gas flow in mudrocks (shales and siltstone). J. Can. Petrol. Technol. 48 (8), 16–21. https://doi.org/10.2118/09-08-16-DA.

Jiang, J., Yang, J., 2018. Coupled fluid flow and geomechanics modeling of stress-sensitive production behavior in fractured shale gas reservoirs. Int. J. Rock Mech. Min. Sci. 101, 1–12. https://doi.org/10.1016/j.ijrmms.2017.11.003.

Karim, M.K., Pierre, G., Jean, B.C., Thierry, J.M., 2022. Modelling stress-induced permeability alterations in sandstones using CT scan-based representations of the pore space morphology. Int. J. Rock Mech. Min. Sci. 150, 104998. https://doi.org/10.1016/j.ijrmms.2021.104998.

Kozhevnikov, E., Turbakov, M., Riabokon, E., Gladkikh, E., Guzev, M., Qi, C., Li, X., 2024. The mechanism of porous reservoir permeability deterioration due to pore pressure decrease. Advances in Geo-Energy Research 13 (2), 96–105. https://doi.org/10.46690/ager.2024.08.04.

Langmuir, I., 1968. The constitution and fundamental properties of solids and liquids. II liquids. In: Leicester, H. (Ed.), A Source Book in Chemistry, 1900-1950. Harvard University Press, Cambridge, MA and London, England, pp. 123–131. https://doi.org/10.4159/harvard.9780674366701.c50.

Li, W., Liu, P., 2023. Novel shale permeability model considering the internal dependencies of effective stress, gas sorption, and flow-regime effects. Energy & Fuels 37 (8), 5777–5791. https://doi.org/10.1021/acs.energyfuels.2c04149.

Li, Z., 2012. Dynamic characteristics of nanoscale pore seepage in shale gas. Nat. Gas. Ind. 32 (4), 1–4. https://doi.org/10.3787/j.issn.1000-0976.2012.04.012 (in Chinese).

Liang, Y., Cheng, Y., Han, Z., Yan, C., 2024. Numerical simulation analysis on production evolution laws in shale reservoirs considering a horizontal well interwell interference effect. Energy & Fuels 38 (5), 4076–4090. https://doi.org/10.1021/acs.energyfuels.3c04951.

Liao, S., Hu, J., Zhang, Y., 2024. Mechanism of hydraulic fracture vertical propagation in deep shale formation based on elastic–plastic model. Eng. Fract. Mech. 295, 109806. https://doi.org/10.1016/j.engfracmech.2023.109806.

Liu, J., Elsworth, D., 1999. Evaluation of pore water pressure fluctuation around an advancing longwall face. Adv. Water Resour. 22 (6), 633–644. https://doi.org/10.1016/S0309-1708(98)00041-4.

Liu, W., Yao, J., Zeng, Q., 2019. Numerical simulation of hydraulic fracture propagation in deep reservoir. Sci. Sin.: Technologica. 49 (2), 223–233. https://doi.org/10.1360/N092017-00207.

Mandel, J., 1953. Consolidation des sols (étude mathématique). J. Geotechnique. 3, 287–299. https://doi.org/10.1680/geot.1953.3.7.287.

Mehrabian, A., Abousleiman, Y., 2015. Gassmann equations and the constitutive relations for multiple-porosity and multiple-permeability poroelasticity with applications to oil and gas shale. Int. J. Numer. Anal. Methods GeoMech. 39 (14), 1547–1569. https://doi.org/10.1002/nag.2399.

Pan, Z., Connell, L.D., 2012. Modelling permeability for coal reservoirs: A review of analytical models and testing data. Int. J. Coal Geol. 92, 1–44. https://doi.org/10.1016/j.coal.2011.12.009.

Qi, S., Tan, X.H., Li, X.P., et al., 2021. Numerical simulation and experimental verification studies on a unified strength theory-based elastoplastic damage constitutive model of shale. Nat. Gas. Ind. 8 (3), 267–277. https://doi.org/10.1016/j.ngib.2021.04.005.

Ran, Q., Gu, X., 1997. Three-dimensional elastoplastic finite element model for dynamic prediction of reservoir effective stress. J. Geomechanics 2, 35–42 (in Chinese).

Shang, X., Zhang, Z., Yang, W., Wang, J.G., Zhai, C., 2022. A thermal-hydraulic-gas-mechanical coupling model on permeability enhancement in heterogeneous shale volume fracturing. Mathematics 10 (19), 3473. https://doi.org/10.3390/math10193473.

Shentu, J., Lin, B., Jin, Y., Yoon, J.S., 2024. Investigation of hydraulic fracture propagation in conglomerate rock using discrete element method and explainable machine learning framework. Acta Geotech 19, 3837–3862. https://doi.org/10.1007/s11440-024-02317-9.

Terzaghi, K., 1943. Theory of consolidation. In: Theoretical Soil Mechanics, pp. 265–296.

Tuncay, K., Corapcioglu, M.Y., 1995. Effective stress principle for saturated fractured porous media. Water Resour. Res. 31 (12), 3103–3106. https://doi.org/10.1029/95WR02764.

Wang, H.N., Guo, Z.Y., Gao, X., Jiang, M.J., 2020. Elastoplastic analytical investigation of mechanical response of wellbore in methane hydrate-bearing sediments. Journal of Tongji University (Natural Science). 48 (12), 1696–1706. https://doi.org/10.11908/j.issn.0253-374x.20127 (in Chinese).

Wang, J., 2020. Experimental study on effect of buried depth of Longmaxi Formation on mechanical properties of shale in southeast Sichuan. Sci. Technol. Eng. 20 (14), 5575–5582 (in Chinese).

Wang, Q., Wang, D., Yu, B., et al., 2024. Evolution of elastic–plastic characteristics of rocks within middle-deep geothermal reservoirs under high temperature. Nat. Resour. Res. 33, 1573–1596. https://doi.org/10.1007/s11053-024-10342-4.

Wang, Y., Liu, S., Zhao, Y., 2018. Modeling of permeability for ultra-tight coal and shale matrix: A multi-mechanistic flow approach. Fuel 232, 60–70. https://doi.org/10.1016/j.fuel.2018.05.128.

Wei, S., Kao, J., Jin, Y., et al., 2021. A discontinuous discrete fracture model for coupled flow and geomechanics based on FEM. J. Petrol. Sci. Eng. 204, 108677. https://doi.org/10.1016/j.petrol.2021.108677.

Wu, K., Chen, Z., Li, X., Guo, C., Wei, M., 2016. A model for multiple transport mechanisms through nanopores of shale gas reservoirs with real gas effect-adsorption-mechanic coupling. Int. J. Heat Mass Tran. 93, 408–426. https://doi.org/10.1016/j.ijheatmasstransfer.2015.10.003.

Wu, Y., Liu, J., Elsworth, D., Siriwardane, H., Miao, X., 2011. Evolution of coal permeability: Contribution of heterogeneous swelling processes. Int. J. Coal Geol. 88 (2–3), 152–162. https://doi.org/10.1016/j.coal.2011.09.002.

Xing, Y., Zhang, G., Li, S., 2020. Thermoplastic constitutive modeling of shale based on temperature-dependent Drucker-Prager plasticity. Int. J. Rock Mech. Min. Sci. 130, 104305. https://doi.org/10.1016/j.ijrmms.2020.104305.

Xu, F.S., Wang, F.P., Zhang, J.T., et al., 2021. Development strategy for the scale and efficiency of deep shale gas in China. Journal of Natural Gas Industry 41 (1), 205–213. https://doi.org/10.3787/j.issn.1000-0976.2021.01.019 (in Chinese).

Xu, P., Yu, B., 2008. Developing a new form of permeability and Kozeny–Carman constant for homogeneous porous media by means of fractal geometry. Adv. Water Resour. 31, 74–81. https://doi.org/10.1016/j.advwatres.2007.06.003.

Yao, J., Huang, C., Liu, W., et al., 2018. Key mechanical issues in deep oil and gas reservoir development. Sci. China Phys. Mech. Astron. 48, 044701. https://doi.org/10.1360/SSPMA2017-00286 (in Chinese).

Yi, D., Yang, Z., Yi, L., et al., 2025. Simulation of dynamic pulse fracturing in elastoplastic media based on a mixed-mode fatigue phase-field model. Comput. Geotech. 179, 107043. https://doi.org/10.1016/j.compgeo.2024.107043.

Yu, R.Z., Wang, C.H., Zhang, X.W., Hu, Z.M., Sun, Y.P., Guo, W., Duan, X.G., Wang, M. Z., 2022. Development characteristics and enlightenment of Eagle Ford deep shale gas reservoirs in North America. Coal Geol. Explor. 50 (9), 32–41. https://doi.org/10.12363/issn.1001-1986.21.12.0815 (in Chinese).

Zeng, Q., Yao, J., Shao, J., 2019. Effect of plastic deformation on hydraulic fracturing with extended element method. Acta Geotech 14, 2083–2101. https://doi.org/10.1007/s11440-018-0748-0.

Zhang, H., 2020. Study on Plastic Zone of Vertical Wellbore. Master's Thesis. Xi'an Shiyou University. https://link.cnki.net/doi/10.27400/d.cnki.gxasc.2020.000156 (in Chinese).

Zhang, H., Liu, J., Elsworth, D., 2008. How sorption-induced matrix deformation affects gas flow in coal seams: A new FE model. Int. J. Rock Mech. Min. Sci. 45, 1226–1236. https://doi.org/10.1016/j.ijrmms.2007.11.007.

Zhang, W., Wang, Q., Ning, Z., Zhang, R., Huang, L., Cheng, Z., 2018. Relationship between the stress sensitivity and pore structure of shale. J. Nat. Gas Sci. Eng. 59, 440–451. https://doi.org/10.1016/j.jngse.2018.09.010.

Zhao, K., Li, R., Feng, Y., et al., 2022. Distribution of plastic zone around horizontal wells in hydrate reservoir in nonuniform in-situ stress field. J. Cent. S. Univ. 53 (3), 952–962. https://doi.org/10.11817/j.issn.1672-7207.2022.03.017 (in Chinese).

Zhao, Y., Lu, G., Zhang, L., Wei, Y., Guo, J., Chang, C., 2020. Numerical simulation of shale gas reservoirs considering discrete fracture network using a coupled multiple transport mechanism and geomechanics model. J. Petrol. Sci. Eng. 195, 107588. https://doi.org/10.1016/j.petrol.2020.107588.

Zhu, W., Chen, Z., Liu, K., 2022. A new meshless method to solve the two-phase thermo-hydro-mechanical multi-physical field coupling problems in shale reservoirs. J. Nat. Gas Sci. Eng. 105, 104683. https://doi.org/10.1016/j.jngse.2022.104683.

Zhu, W., Chen, Z., He, X., Tian, Z., Wang, M., 2023. Numerical investigation of influential factors in hydraulic fracturing processes using coupled discrete element-lattice Boltzmann method. J. Geophys. Res. Solid Earth 128, e2023JB027292. https://doi.org/10.1029/2023JB027292.